Check for updates

Mid-infrared optical coherence tomography as a method for inspection and quality assurance in ceramics additive manufacturing

Ivan Zorin [a],[*], Dominik Brouczek [b], Sebastian Geier [b], Serkan Nohut [b],[c], Julia Eichelseder [b], Guillaume Huss [d], Martin Schwentenwein [b], Bettina Heise [a]

[a] Research Center for Non-Destructive Testing GmbH, Science Park 2, Altenberger Str.69, Linz, 4040, Austria
[b] Lithoz GmbH, Mollardgasse 85a/2/64-69, Vienna, 1060, Austria
[c] Piri Reis University, Department of Mechanical Engineering, Postane Mah. Eflatun Sok. 8, Istanbul, 34940, Turkey
[d] LEUKOS SAS, 2 rue Edouard Michaud, Limoges, 87000, France

ARTICLE INFO

ABSTRACT

In the past decade, significant progress has been made in ceramics additive manufacturing (AM). Material research and the rapid evolution of high-resolution printing technologies enabled the production of high-quality, high-precision, complex-structured ceramic objects. In this contribution, we propose a contactless, non-destructive method of mid-infrared optical coherence tomography (mid-IR OCT) for at-line inspection and quality assurance of AM ceramics. The OCT system operates in the spectral range from 3.15 μm to 4.2 μm featuring extended probing depth into porous ceramics. The spatial resolution of the mid-IR OCT system is suited to most of AM techniques: the axial resolution (determined by the coherence length) is 8 μm; the lateral resolution is around 40 μm (determined by the size of the focused beam). The capabilities of the method are demonstrated by imaging diverse high-scattering single and multi-component samples (in both green and sintered states) fabricated by means of lithography-based ceramics manufacturing. The selected materials are alumina and zirconia, the gold standard in AM. Some features of interest, such as local changes in porosity, surface and sub-surface defects and layer structure, were accessed and analyzed.

1. Introduction

Ceramic additive manufacturing (AM) has developed rapidly in recent years, as evidenced by its significant impact on the industry and extensive scientific reports [1–4]. High-performance ceramic materials employed in AM have unique and diverse properties. They possess bending and tensile strength, high density, corrosion, chemical, and thermodynamic stability; optical properties include broad spectral response, strong scattering, and high damage threshold. Some materials exhibit specific thermal and electrical properties (insulation or conductivity), or, for instance, piezoelectric characteristics [5,6]. Due to this variety of material characteristics, three-dimensional (3D) ceramic printing technology has aroused great interest in various applied scenarios. The ceramic AM systems became commercial and found wide adoption in fields ranging from biomedicine (especially application of so-called bio-ceramics for implant printing and bone tissue engineering) [7–14], to, for instance, terahertz technology [15–17], microelectronics [18–20], automotive and aerospace industries [21,22]. Nevertheless,

despite the seeming maturity of the technology, 3D ceramic printing is still in an intensive development phase. The main focus is on material research and optimization of the printing process, dimensional accuracy, and minimization of defects (such as cracking, contamination, delamination, surface and sub-surface inhomogeneities, surface quality, shrinkage etc.) [23].

Various inspection, characterization and quality control methods are used to obtain the relevant data required to study materials and optimize the printing process. Probably the most common techniques for morphological evaluation are scanning electron microscopy, X-ray imaging (micro-computed tomography), and optical microscopy; porosity analysis — another important quantity for AM of ceramics — is usually performed conventionally using the Archimedes method or gravimetric approaches. Scanning electron microscopy provides extremely high resolution, allowing evaluation of surface quality, roughness and average pore size; the application, however, is confined to the examination of the sample surface [24]. X-ray tomographic imaging techniques enable volumetric morphological imaging with high spatial

resolution, albeit with long processing times [25]. The chamber size of standard micro-computed tomography systems limits their use for relatively small samples or involves cutting out fragments for examination [26]. Besides, X-rays are ionizing, which restricts their use in certain scenarios. Apart from the high capital costs of both methods, both X-ray methods and scanning electron microscopy are technically complex, so they are not feasible for at- and even less so for in-line monitoring. In contrast, conventional optical microscopy is cost-effective and technically simple, but merely limited in performance. Thus, only surface analysis (due to scattering and absorption) with confined spatial resolution and depth of field is possible [27]. The classical methods of porosity analysis mentioned above are conventional manual procedures that provide average sample porosity without any spatial localization.

An alternative method that is not as commonly known in the ceramic community, but is well suited for assurance, qualitative and quantitative control, and dimensional metrology, is optical coherence tomography (OCT). OCT is a well-established non-destructive and contactless method for 3D structural imaging of complex-shaped turbid specimens [28]. OCT operates as an optical length gauge and uses optical interferometric detection (i.e. signals are coherently amplified) of backscattered light, which enables depth discrimination capability. OCT systems are relatively cost-effective, reliable, and provide high sensitivities (sensitivity above 110 dB can be achieved [29]) and high-speed data acquisition (MHz rates reported [30–32]). The usual imaging depth of OCT systems ranges from hundreds of micrometers to a couple of millimeters. OCT enables defectoscopy, direct quantitative and qualitative morphological imaging and indirect analysis of various optical material responses. For this reason, notable solutions span various fields of research. The main areas of the application are biomedicine and ophthalmology [33,34]. However, there is a wide variety of prominent use cases for non-destructive testing beyond the biomedical applications standard for OCT [35–38]. Among them are several reports on the application of near-infrared (near-IR) OCT systems to the inspection of ceramic materials also covering AM scenarios [39–42]. Thus, the performances of OCT to evaluate geometry, analyze particle or grain composition and distribution, map localized porosity, surface topology, and defectoscopy are in principle known and practically studied. However, it is essential to note that most industrial ceramics are challenging materials for state-of-the-art OCT systems —standard commercial systems operate in the well-developed near-IR spectral range, at most at wavelengths up to 1.5 μm. In this spectral window, ceramic media exhibit strong elastic light scattering, so the probing depth is severely constrained.

Scattering in ceramics with an emphasis on OCT imaging, as well as the search for an optimal spectral band was first theoretically investigated by R. Su et al. in Ref. [43]. A significant increase in OCT penetration depth was predicted to be at longer wavelengths, i.e. in the mid-IR spectral range between 2 μm and 4 μm. This wavelength range also provides a good compromise with axial resolution in comparison to e.g. THz solutions [44]. Thus, the simulations have shown that the optimal spectral range provides increased tolerance to scattering as its magnitude decreases with increasing wavelength [45,46]. In the last few years, the predictions of R. Su et al. have been confirmed by several research groups when the first mid-IR OCT systems were experimentally demonstrated [47,48]. It has been verified, that the imaging performance of mid-IR OCT for industrial porous ceramics can be substantially improved compared to that of near-IR systems. These first experimental reports were followed by derivative publications addressing further developments of mid-IR OCT systems; some potential applications were identified [49–54].

In this contribution, we introduce mid-IR OCT as an alternative and promising tool for at-line volumetric imaging, inspection, material research, and quality assurance in 3D ceramics printing. We demonstrate the capabilities of this technology to the broad community dealing with material research and development of AM machinery. Thus, the experimental part includes measurements of various high-scattering AM ceramic samples (single- and multi-component) in both green and sintered states. We present the system's capabilities for defectoscopy, dimensional metrology (surface and sub-surface features), and localization of porosity variations for 3D printed ceramics. The investigated samples were produced by the method of lithography-based ceramic manufacturing (LCM).

2. Material and methods

2.1. Mid-infrared spectral-domain optical coherence tomography system

The mid-IR OCT system employed for at-line measurements of 3D-printed ceramics is schematically shown in Fig. 1. The setup consists of three core units: a compact measurement head (size 16.5 cm×12.5 cm×6 cm), a detection system (dispersive single-pixel scanning spectrometer), and a mid-IR supercontinuum source. The OCT system operates in the spectral domain configuration; the operational spectral window ranges from around 3.15 μm to 4.2 μm. The detection approach relies on time-encoded sampling of spectral interferograms — the OCT signals required to reconstruct morphological information are recorded in time as the spectral components are scanned over a point detector. This is accomplished in the detection module by using a two-fold spectrometer configuration with a $4f$ mirror system (formed by spherical mirrors with focal lengths of 100 mm) that conjugates the grating and scanner planes.

The at-line spectral-domain OCT system is a customized design that has been previously reported in Ref. [55], thus, details on the technical implementation of the system and its characterization can be found in this publication. In terms of system architecture, two technical aspects have been modified. Instead of an all-free-space configuration presented in Ref. [55], in the at-line OCT setup shown in Fig. 1, the core modules of the OCT system are separated by optical fibers for practical flexibility. In addition, the spectrometer's long focal-length focusing optics was replaced with a spherical mirror with a focal length of 150 mm, which allowed us to reduce the size of the detection spectrometer (30 cm×30 cm×20 cm). In order to preserve spectral resolution, since the replaced optics affected linear dispersion, a fixed 100 μm slit (Thorlabs, S100K) was installed in front of the detector. Scanning parameters were adjusted, so that this upgrade impacted the dimensions, and the spectrometer specifications (spectral resolution of around 2 nm) and bandwidth were retained.

The compact measuring head is intended to probe a sample mounted on a two-dimensional motorized scanning stage. The supercontinuum laser light is focused onto the sample; area mapping is performed in a stepwise manner by scanning the beam over the surface of the sample. The measurement head has input and output collimators (cIN and cOUT) to couple light in and out. The input spectral filtering is performed by an edge-pass filter (SF, 2.4 μm cut-on wavelength to block near-IR emission). The core of the head is a Michelson interferometer formed by a pellicle beamsplitter (BS). For focusing, a BaF_2 lens is used (50 mm, dispersion in the interferometer reference arm is compensated by a corresponding BaF_2 window [Comp. in Fig. 1]). This module has been designed so that it can potentially be integrated into AM machinery and used in an in-line monitoring configuration.

The necessary electronics such as a galvo-scanner control unit, a specifically designed single-board boxcar integrator, and a digitizer (14-bit, 125 MS/s sampling rate, 60 MHz bandwidth) are integrated into the detection unit. The system is connected to a PC via Ethernet and is controlled using a graphical user interface.

For OCT imaging, two different mid-IR supercontinuum laser sources were used. The sources can be easily switched since optical fibers are used. For the experimental demonstration, a high-power (about 230 mW average power after the spectral filter) high repetition rate (250 kHz) mid-IR supercontinuum source based on InF_3 fiber was used. This source was specially developed and adapted for this application by Leukos SAS.
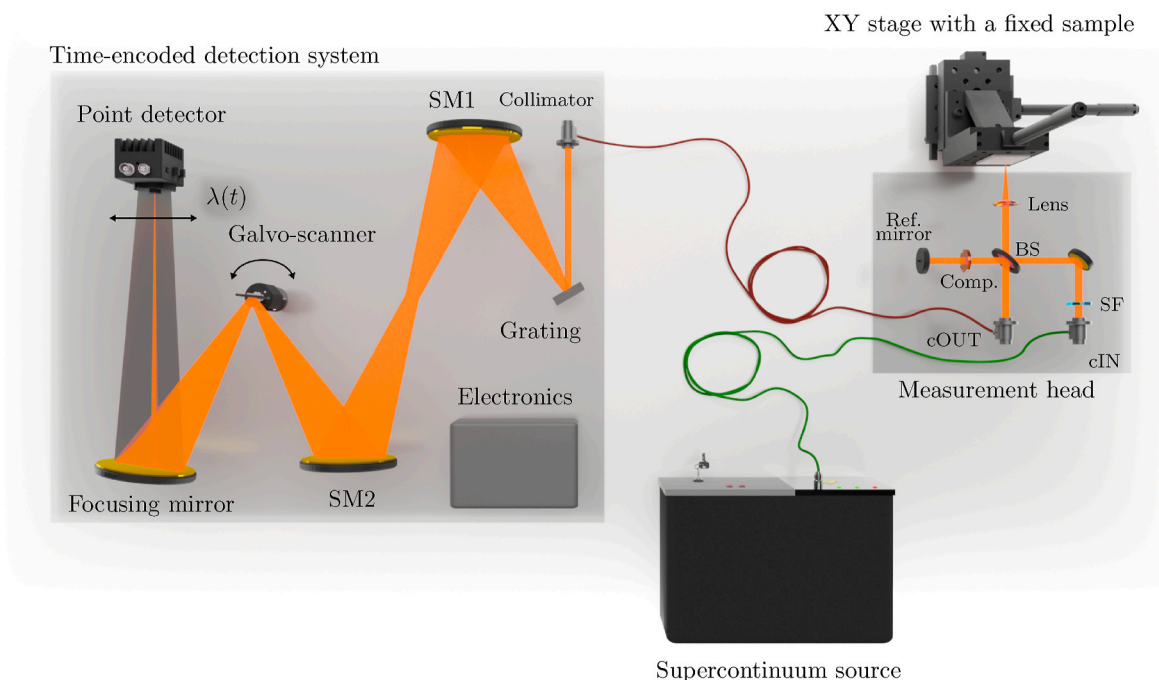
Fig. 1. Basic layout of the at-line mid-IR OCT system that consists of three core units connected by InF₃ fibers for practical versatility; the mid-IR supercontinuum laser source is coupled to the measurement head using an input mirror collimator (cIN); the compact measurement head (containing a spectral filter SF, a Michelson interferometer [BS is a pellicle beam splitter], compensator [Comp., BaF₂ window] and focusing optics) probes the sample fixed in the XY scanning stage; back-scattered and reference beams are collected by an output mirror collimator (cOUT) and redirected to the detection module — a dispersive scanning spectrometer formed by a 4f system (composed of spherical mirrors SM1 and SM2), galvo-scanner and a single point detector; the spectral interferograms are being recorded in time, processed and digitized by the read-out electronics (a boxcar integrator and 14-bit digitizer).

The spectral shape, as well as pulse emission parameters, were optimized for the at-line system providing higher axial resolution. Besides, for power-sensitive applications such as measurements of green parts (since polymer matrix can absorb mid-IR radiation causing thermal load), a low power (16 mW average power after the spectral filter, 40 kHz repetition rate) supercontinuum source from NKT Photonics was used. The axial resolution (in depth direction) of the system that depends on the spectral bandwidth (determined by the coherence length) is around 8 μm (16 μm for the low-power laser source) as was characterized in Ref. [55]; the lateral resolution of the system, determined by the focusing optics (determined by the size of the focused beam), is around 40 μm [49]. Since the axial and lateral components are in general decoupled one from another, the three-dimensional point-spread function has an ellipsoid shape. Specimen structures of the size larger than the spatial resolution can be unambiguously imaged and separated; higher spatial frequencies are being suppressed. The resolution is conventionally determined at the full width at half maximum level of the point spread function [28]. The sensitivity of the system is around 80.17 dB, which allows to distinguish reflectivities or reflectivity variations lower than $R = 10^{-8}$ (in free space in the absence of scattering). The A-scan rate was set to 50 Hz for all the measurements, i.e. the time required to map a single point withing the region of interest is 20 ms. The effective imaging depth range of the system, set by the confocal gate of the focusing optics, is around 1.1 mm. Both the Nyquist-limited depth range (>16 mm due to digitization of spectral interferograms) and the 6 dB range (about 1.4 mm due to sensitivity roll-off) are not limiting factors for the presented design [28].

2.2. Lithography-based ceramics manufacturing machinery

The components produced via LCM-technology were printed with two different types of devices. The parts consisting of one material were printed with the CeraFab 7500 and the specimens containing two different materials were printed with the CeraFab Multi 2M30. The pixel size defines the lateral resolution and is 40×40 μm² for both devices; thus, the resolution of the developed mid-IR OCT system is optimally matched to the printing equipment used. The schematic setup of these
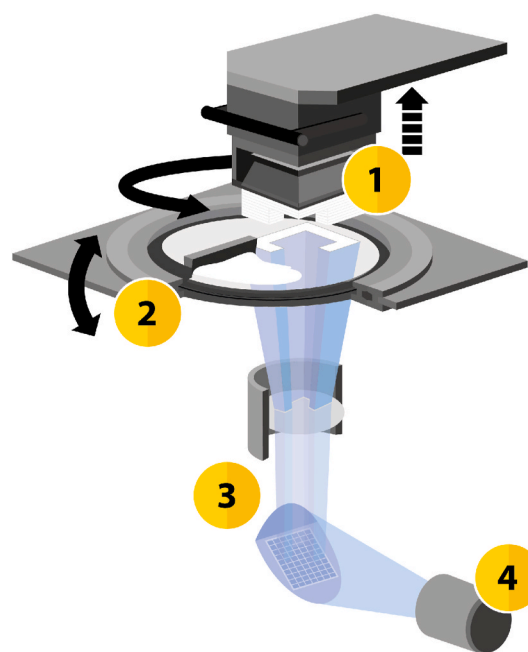

Fig. 2. Schematic structure of the CeraFab printers. (1) build platform, which is movable in Z-direction; (2) rotatable vat, in which the material is deposited; (3) optical system, which transmits the light from the LED lamp (4) to the projection surface, generating selective layer images.

printers is essentially the same and is shown in Fig. 2.

The 3D design to be printed is uploaded in STL format and divided into 2D images by the machine software. The number of images generated depends on the selected layer thickness (corresponds to the thickness of a printed layer). During 3D printing, the ceramic-loaded suspension (or slurry) is automatically dispensed and applied to a transparent vat. The movable build platform is immersed in the slurry, which is then selectively exposed to visible light from below. The layer image is generated using a digital micromirror device (DMD) in conjunction with a state-of-the-art projection system. By repeating this process, a three-dimensional green body can be created layer by layer. This so-called green body consists of ceramic particles embedded in a polymer matrix. The matrix is removed from the green body during debinding by thermal treatment up to 600 °C. Through a further thermal treatment at high temperatures, the sintering process, the porous body is compacted and densified, which means that the originally loose powder is transformed into a dense, solid ceramic part, leading to a dimensional change due to shrinkage.

2.3. Samples: lithography-based manufactured ceramics

In order to demonstrate the capabilities and performance of mid-IR OCT to investigate diverse features of high-scattering 3D printed ceramics, several samples with specific traits were selected. It should be noted, that selected materials are the most used for AM. The performance of OCT (and mid-IR OCT in particular) for materials such as hydroxyapatite, silicon nitride, or silicon carbide can be affected due to e.g. increased absorption or high dispersion [56–59]. Fig. 3 displays the visible photos of the test samples.

2.3.1. Alumina plate with surface and sub-surface defects due to contamination

The sample is a thick plate of a single material, see Fig. 3a. The part was printed vertically. It is a sintered alumina plate, with a dimension of $25 \times 2 \times 25$ mm^3. The part was produced with a layer thickness of 25 µm

(total number of layers 1280). The exposure energy was set to 150 mJ/cm^2. During the sintering process in the furnace, the sample encountered a foreign material, which resulted in these punctual foreign phase impurities on the surface.

The defects aroused due to contamination are of interest for morphological analysis, i.e. to analyze its penetration into the bulk body, as well as for indirect analysis of density inhomogeneities (porosity mapping).

The thickness of the plate is outside of the imaging depth of the OCT system, thus, the back interface was not expected to be accessed.

2.3.2. Plates structured by dense and porous alumina ceramics (2-component parts, green and sintered)

Porosity gradient alumina samples were produced with a discrete material transition on a lateral plane perpendicular to the deposition direction. The newly developed multi-material LCM printer CeraFab Multi 2M30 was employed for the production. The green body and sintered parts are shown in Fig. 3b and c correspondingly. With the help of a within-layer approach, it is possible to use two different materials on the same layer [60]. For the fabrication of porosity graded alumina samples, commercially available alumina slurry LithaLox 350 (Lithoz GmbH, Austria) with a volumetric alumina powder content of 49% was used. PMMA microbeads with the particle size distribution of $d_{50} = 8$ ~11 µm were used as pore-forming agents (PFA) for the fabrication of porous alumina regions. The samples are structured in such a way that the density varies along one dimension between the two end surfaces of dense and porous with expected porosities of 10% and 30%. The width of one material region to another increased incrementally along the axis of interest as 105 µm, 210 µm, 315 µm, 430 µm, 525 µm, 525 µm, 630 µm, 735 µm, 840 µm, 945 µm, 1400 µm. All layers were printed with 25 µm layer thickness by exposing both materials to 150 mJ/cm^2 by using a mono-chromatic (450 nm) projector with a power of 50 mW/cm^2.

The waiting times before curing the layers were selected 15 s. The post-processing cleaning was performed by using the solution LithaSol20 (Lithoz GmbH, Austria) and compressed air. The samples were
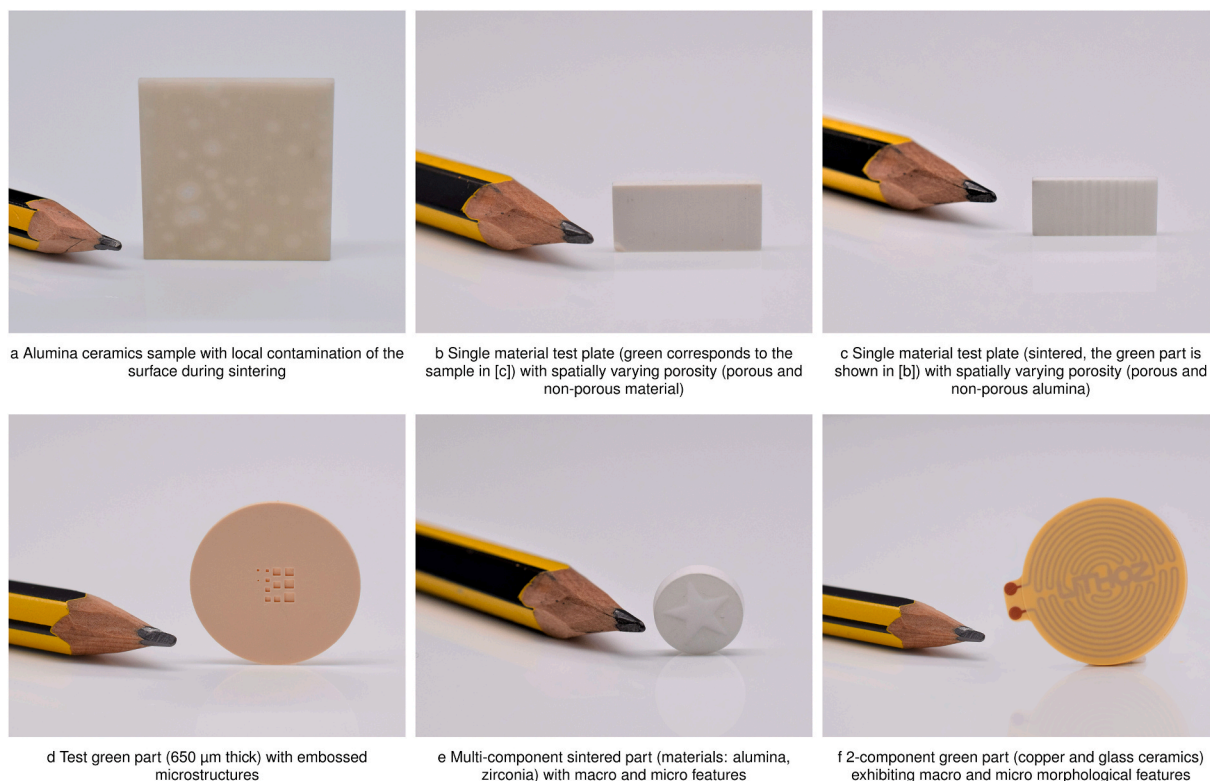

a Alumina ceramics sample with local contamination of the surface during sintering

b Single material test plate (green corresponds to the sample in [c]) with spatially varying porosity (porous and non-porous material)

c Single material test plate (sintered, the green part is shown in [b]) with spatially varying porosity (porous and non-porous alumina)

d Test green part (650 µm thick) with embossed microstructures

e Multi-component sintered part (materials: alumina, zirconia) with macro and micro features

f 2-component green part (copper and glass ceramics) exhibiting macro and micro morphological features

Fig. 3. Samples used for experimental demonstrations; each sample possesses specific features of interest.

sintered at 1650 °C for 2 h with a heating rate of 1 °C/min. The total thickness of the samples was measured as approximately 1.3 mm and 1.0 mm for the green body and sintered states. In this article, both green and sintered parts were examined with the mid-IR OCT system to display the capabilities to investigate complex porosity profiles of 3D printed ceramic parts.

2.3.3. Microstructured green alumina disk with embossed surface pattern

This green-state sample [Fig. 3d] with a centered pattern was specifically designed for OCT imaging to demonstrate the increased penetration depth and capabilities of the mid-IR OCT system for structural imaging and volumetric dimensional metrology.

The disk was printed horizontally. The component has a diameter of 18.3 mm and a thickness of 650 μm. The part was printed with a layer thickness of 25 μm (total amount of layers 26) and an exposure energy of 500 mJ/cm^2. The depth of the pattern is 325 μm. The centered pattern consists of squares of varying sizes: sides of 1.2 mm, 1.12 mm, 1.04 m, 0.96 mm, 0.88 mm, 0.80 mm, 0.72 mm, 0.64 mm, 0.56 mm, 0.48 mm, 0.40 mm, 0.32 mm, 0.24 mm, 0.1 mm.

2.3.4. Bulk sintered 2-component part with a star pattern

The sample [Fig. 3e] is composed of two materials. The star pattern in the centre of the sample is zirconia ceramic; the rest is printed with alumina ceramic. The sample was manufactured with the following parameters: layer height of 25 μm; exposure energy 150 mJ/cm^2 for both components; sintering temperature was 1450 °C. At this temperature, zirconia is densely sintered. The standard sintering temperature for alumina is 1600 °C. For this reason it can be assumed that its density is slightly lower (an estimated relative density of 95%).

The sample has both structural (shape deviation due to different shrinkage of the materials, layer thickness) and material (different density) features.

The thickness of the sample is 3 mm, i.e. outside of the mid-IR OCT imaging range, thus, the back interface is not accessible.

2.3.5. 2-Component Cu/glass ceramic green part with a complex 3D structure

The sample consists of 2 materials, see Fig. 3f. The main body is made of glass-ceramic combined with an embedded copper layer. The sample is a green part, thus consists of a polymer matrix with embedded copper and ceramic particles with an respective layer heights of 30 μm. Glass-ceramic, which is the insulating part, can be used for the production of ceramic green parts which are processed by LTCC (Low Temperature Co-fired Ceramics)—technology to generate metal-ceramic structures for the electronic industry: for example printed circuit boards, piezo-electric stacks, electronic and telecommunication components. Glass-ceramics are used due to their properties, such as low melting temperature, low thermal expansion coefficient, high resistance, and surface tension [61–63]. The copper layer (conductive tracks), which represents the conductive part, is then covered with 3 layers (90 μm) of glass-ceramics. In this way, a complex multimaterial 3D structure is formed. The part around the "Lithoz" lettering is selected for the scan. The sample has both surface and sub-surface features. The 1.5 mm high sample with a diameter of 20 mm has been printed with 30 μm layer thickness. The exposure energy for the copper was 2000 mJ/cm^2; and for the glass-ceramic 400 mJ/cm^2. This sample possesses varying material properties, which provide suitable contrasts for OCT imaging. Besides, the imaging of the present structural features is of practical interest.

3. Results

This section presents experimental results and their interpretation, showcasing the system's performance. All the OCT scans provided are in logarithmic scale and are rendered in grayscale (colour bar scale units are decibels, given on the left side of the B-scans), with the areas of
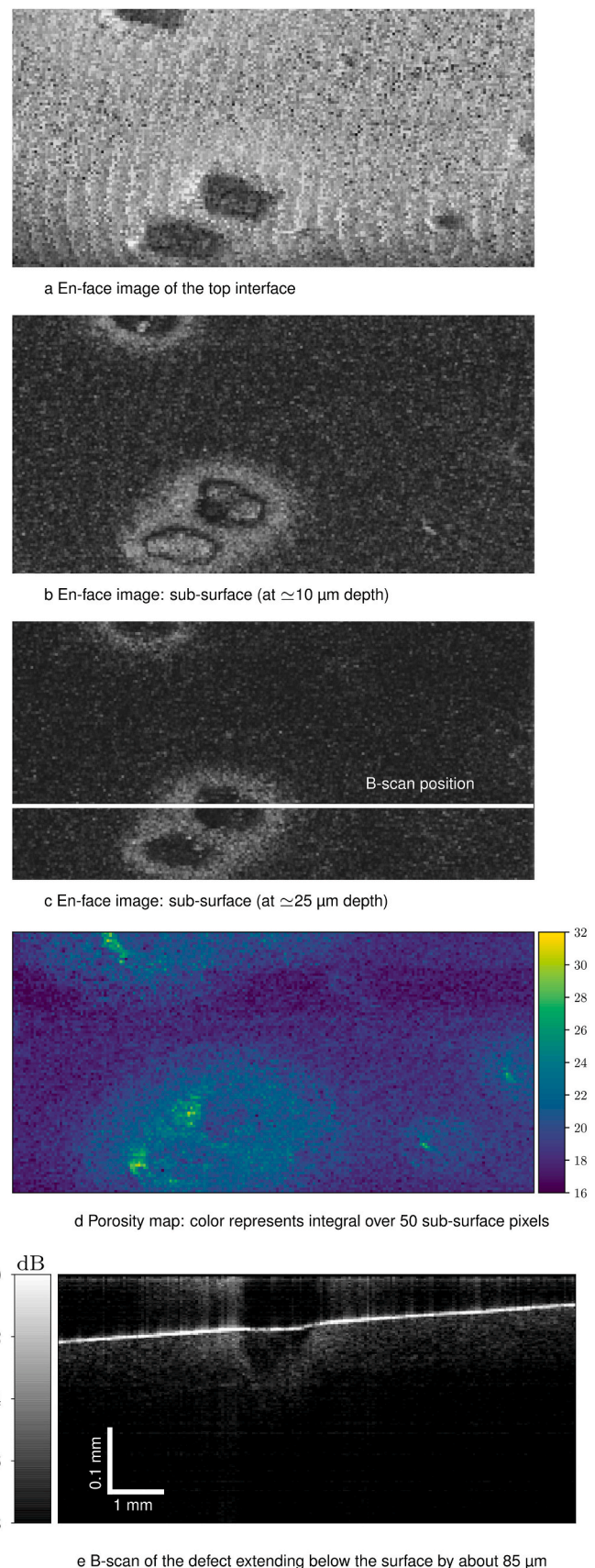

a En-face image of the top interface

b En-face image: sub-surface (at ≃10 μm depth)

c En-face image: sub-surface (at ≃25 μm depth)

d Porosity map: color represents integral over 50 sub-surface pixels

e B-scan of the defect extending below the surface by about 85 μm

Fig. 4. OCT examination of the plate with surface and sub-surface defects due to the contamination; a volumetric scan of 10×5 mm^2 is analyzed in (a–d).

stronger reflection whiter. Essential information about the obtained images (i.e. dimensions of en-face sections) is indicated in the captions; the positions of the cross-sectional scans (so-called B-scans) are specified for ease of comprehension; each B-scan features calibrated dimensional bars.

The porosity maps obtained for some samples are aimed at qualitative analysis and localization of material density and are derived from volumetric scans by integrating the scattering decay profile in a fixed range below the upper interface. Hence, the color space of the porosity maps codes a corresponding integral.

Fig. 4 depicts processed OCT measurements of the thick sintered alumina plate with surface and sub-surface defects due to contamination. The top surface of the specimen is shown in the en-face scan in Fig. 4a (10×5 mm^2, XY lateral section of the volumetric scan). The striped structure superimposed on the image is due to interference effects resulting from a slight tilt of the sample. The en-face image clearly reveals contaminated areas, minor surface defects, as well as small height variations in areas of the impurities. An en-face scan, taken 10 μm below the upper interface, shows the top interface of the heterogeneities as they are brighter (see Fig. 4b). Thus, the defects affect the shape of top interface and slightly distort it.

Further volumetric analysis shows that the inhomogeneities exhibit different penetration into the main intact body. An en-face scan at a depth of approximately 25 μm below the surface (see Fig. 4c) displays that the two small defects visible on the right side of the scans on Fig. 4a and b are not present at this depth.

The penetration profile can be more efficiently assessed using a B-scan through one of the defects. Fig. 4e depicts a cross-section of a defect (B-scan is orthogonal to the en-face images shown), which shows that the defect volume extends below the surface by about 85 μm. The Z depth axis has been calibrated using a group refractive index of alumina [64].

In addition, it can be observed that the defects show reduced scattering compared to the intact body, as the speckle pattern is less pronounced and the image colour is more homogeneous in the centre of the heterogeneity. At the same time, a clear scattering aureole (brighter regions around the impurities) is well visible, which in contrast can be associated with increased scattering. Thus, the test sample possesses a local variation in porosity, which can be accessed by additional processing of the volumetric scan. Fig. 4d depicts a porosity map obtained for this sample. The aforementioned theses are supported by this analysis, since the brighter areas of the map correspond to more porous regions of the sample, as light scattering increases with the number of scatterers [46] (e.g., air bubbles, microscopic cracks, etc.). Thus, concerning the sintering process of this ceramic part, the conclusion of the analysis confirm that the sample was locally overheated. The source of these inclusions was a contaminated sintering furnace in which the samples were in contact with foreign material.

Mid-IR OCT imaging and analysis of green and sintered plates structured by dense and porous alumina ceramics are shown in Figs. 5 and 6 correspondingly. The green part exhibit distinct height differences between the dense and porous components, which can be seen in the images of the structure from the front side (seeFig. 5a and b) and clearly accessible in a B-scan shown in Fig. 5d. In addition, small irregularities and defects in the stripes can be observed in both en-faces.

Besides, the B-scan, which provides a sufficient signal up to around 180 μm in depth, reveals the individual printing layers for the porous component strips (observable as horizontal lines). Thus, the transition between the layers of the porous component is not homogeneous causing back-scattering at the layer-to-layer interface; the estimated layer thickness is around 20 μm (slight discrepancy is possible, because the Z-axis is calibrated by the group index of sintered alumina, as the group index of green material is unknown).

The porosity map of the sintered part shown in Fig. 5c enables distinct discrimination of the materials. A porosity profile shown below the map (integral of the map along the Y axis) visualizes the varying
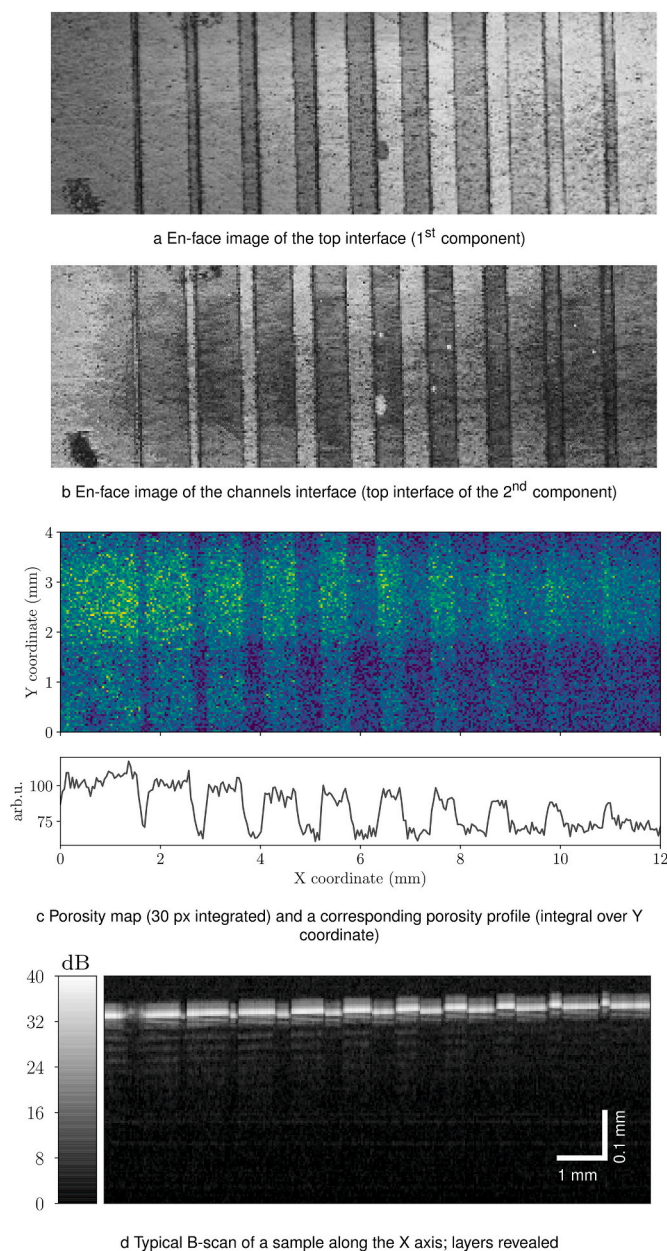

a En-face image of the top interface (1st component)

b En-face image of the channels interface (top interface of the 2nd component)

c Porosity map (30 px integrated) and a corresponding porosity profile (integral over Y coordinate)

d Typical B-scan of a sample along the X axis; layers revealed

Fig. 5. OCT examination and porosity mapping of the green 2-component part with stepwise alternating porosity; a volumetric scan of 12×4 mm^2 is analyzed in (a–c).

density and provides sufficient contrast and signal-to-noise ratio. The edges of the profile are slightly smoothed as the structure is inclined.

In contrast to the green part, the en-face scan for the sintered part depicted in Fig. 6a shows that the height variation between the components becomes negligible after the sintering process. At the same time, the porosity map (Fig. 6b) preserves the designed density profile. Cross-sectional scans of the sintered part are not shown, as no essential information is observable, and the layers could not be detected after sintering. Thus, the sintering process smoothes out heterogeneities between individual layers and increases their interdiffusion.

OCT examination of the test green alumina disk with an embossed surface pattern is shown in Fig. 7. Fig. 7a–d displays the en-face scans at key interfaces of interest: the top surface of the sample, an image of the 5th layer, an image of the pattern face, and an image of the back side respectively.

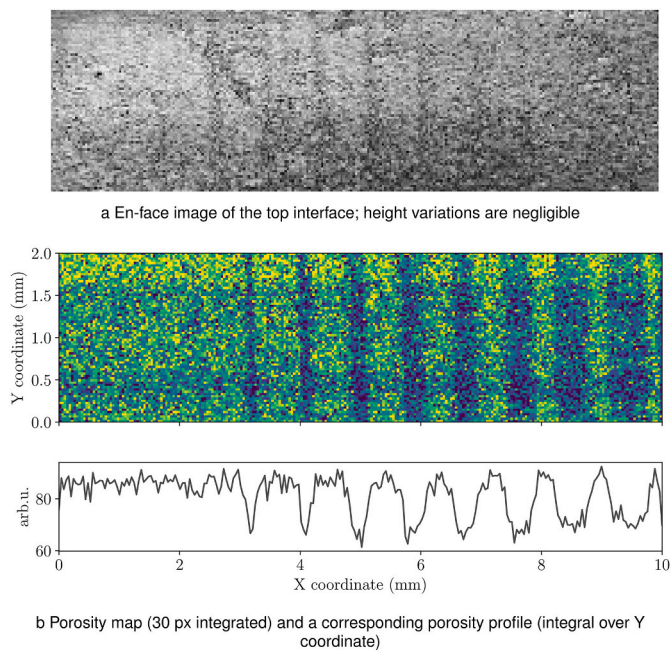The sample has a crack passing through the entire volume that is well

a En-face image of the top interface; height variations are negligible

b Porosity map (30 px integrated) and a corresponding porosity profile (integral over Y coordinate)

Fig. 6. OCT examination and porosity mapping of the sintered 2-component part with stepwise alternating porosity (green part is analyzed in Fig. 5); a volumetric scan of 12×2 mm^2 is analyzed.

visible on all the frontal scans. Such a crack will result in reduced mechanical stability of the part. The top interface has a bubble-type defect on the left side (see Fig. 7a). Such defects are caused by the fact that the sample was printed horizontally and, given its large transverse size, air bubbles cannot always be sufficiently removed during printing.

The en-face of the 5th layer (Fig. 7b) at around 120 μm in depth exhibit scattering irregularities (darker regions, lines) that are not visible on the surface. This can be explained as the printer's vat probably had slight irregularities (e.g. scratches) and was therefore not completely planar. Also, the areas around the pattern are noticeably darker, which in turn reflects the fact that the density is not uniform and probably modulated by the structure, since the local exposure to the light can be not even.

The scan of the pattern interface (Fig. 7c) provides an access to evaluate the quality of the embossed structures, for instance, the edge and angle quality can be further characterized. In addition, it can be noted that the smallest structures do not match the designed thickness and collapse at lower depths because their interface is not identified.

It should be noted that the OCT image of the rear interface of this test specimen, obtained at a maximum depth of about 650 μm, still provides sufficient contrast, as can be seen in Fig. 7d.

Since the supercontinuum beam propagating through the sample and back is used for sensing, this en-face image accumulates some strong features for the preceding layers that affect the beam, for example, the bubble from the top interface can be parsed.

As can be seen, the entire 650 μm thick disc volume was successfully probed using the developed mid-IR OCT system. The printed layers are detected and well pronounced in the B-scan shown in Fig. 7e. Subsurface defects similar to the aforementioned bubble-type surface defect can be identified in the layers (some defects are indicated in the images). The darker area on the B-scan at a depth of about 325 μm corresponds to the position of the pattern (pattern proximity region). No layers are observable in this section, as the material appeared to be more homogeneous in this segment as discussed previously.

In order to stress the increased capabilities of the developed mid-IR OCT for examination of 3D printed ceramic samples, we present comparative measurements for the disk sample. Fig. 7f depicts a B-scan obtained with a state-of-the-art commercial OCT system operating at the
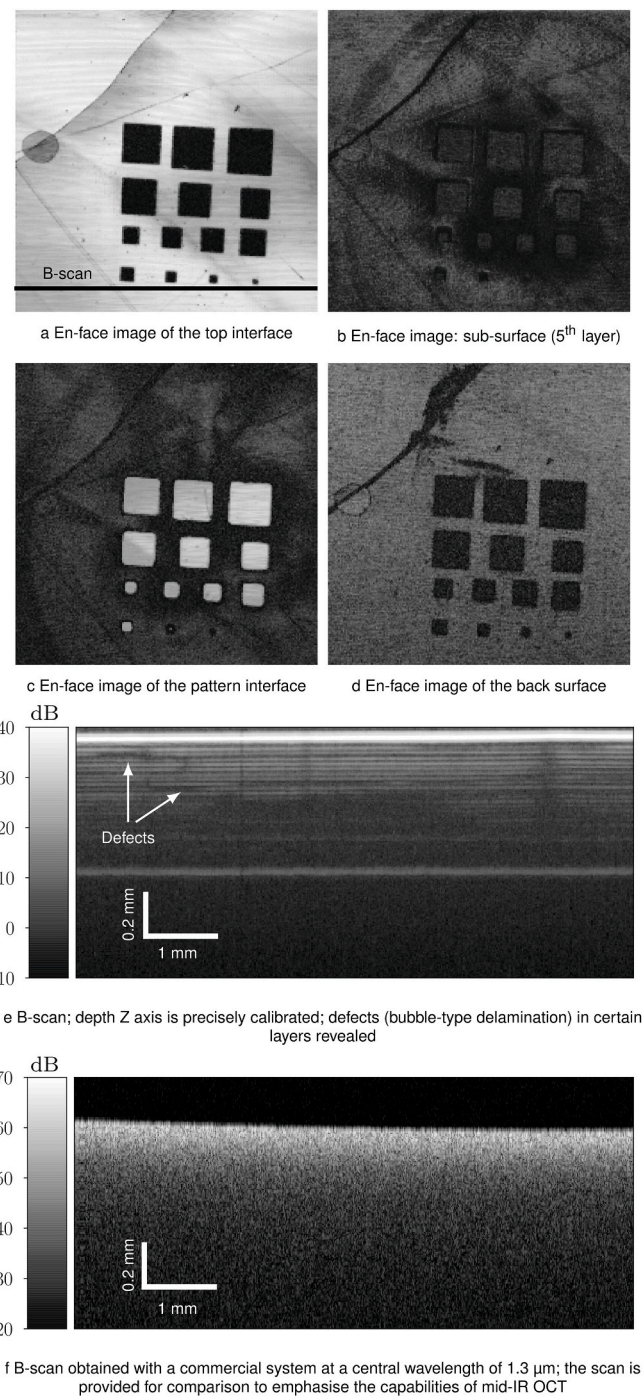

a En-face image of the top interface

b En-face image: sub-surface (5th layer)

c En-face image of the pattern interface

d En-face image of the back surface

e B-scan; depth Z axis is precisely calibrated; defects (bubble-type delamination) in certain layers revealed

f B-scan obtained with a commercial system at a central wavelength of 1.3 μm; the scan is provided for comparison to emphasise the capabilities of mid-IR OCT

Fig. 7. OCT imaging (8×8 mm^2 for en-face scans in [a-d]) of the green state disk sample with a relief pattern and various defects (cracks, bubbles). The layers are revealed in the B-scan (c); the B-scan (f) was captured with a commercial system and shown for comparison.

central wavelength of 1.3 μm (Thorlabs, Vega SS-OCT system, 102 dB sensitivity). The same region as shown in Fig. 7e was measured. The subsurface structure is completely indistinguishable; no layers or interfaces can be observed. The B-scan contains only a characteristic pattern of multiple scattering. Thus, these comparative measurements confirm the increased efficiency of mid-IR OCT for studying samples with high porosity, which includes various 3D-printed ceramics.

A volumetric OCT study of the sintered 2-component part with a star pattern is shown in Fig. 8. The measurements presented include two en-face images (component interfaces), a porosity map, a full volumetric
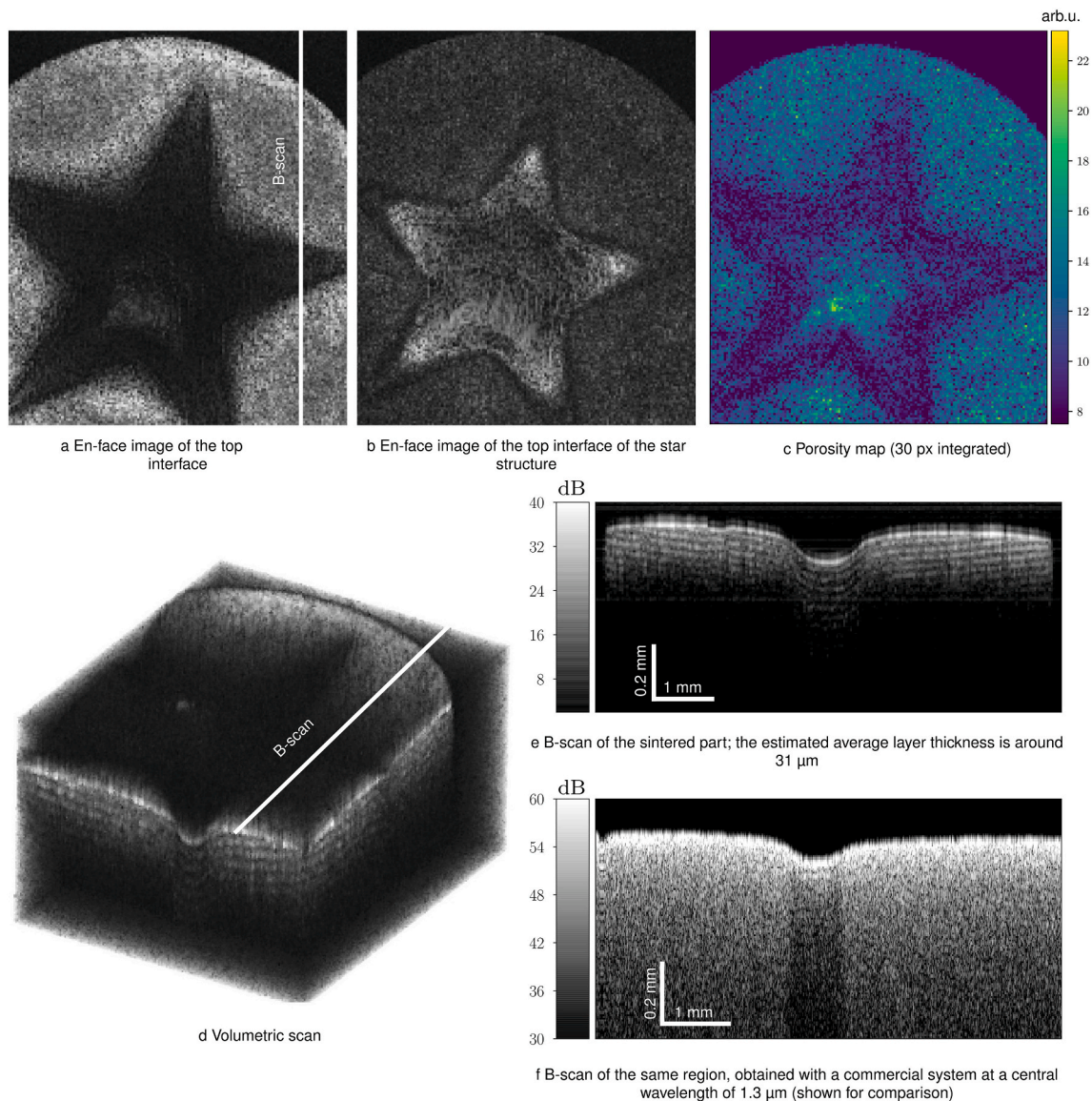
a En-face image of the top interface

b En-face image of the top interface of the star structure

c Porosity map (30 px integrated)

d Volumetric scan

e B-scan of the sintered part; the estimated average layer thickness is around 31 μm

f B-scan of the same region, obtained with a commercial system at a central wavelength of 1.3 μm (shown for comparison)

Fig. 8. OCT imaging (7×6 mm^2 for en-face and volumetric scans as well as for the porosity map [a-c]) of the sintered 2-components part with a star pattern, showcasing various structural features. The layers are revealed in the B-scan (e); the B-scan (f) captured with a commercial system is shown for comparison.

scan, and a typical B-scan.

Since the materials have different shrinkage upon the heat treatment, after sintering the sample acquired a wavy shape. The distorted shape is well-visible in the volumetric scan (Fig. 8d) as well as in the B-scan (Fig. 8e).

The en-face images—Fig. 8a and b—are taken the interfaces of the alumina and zirconia regions respectively enabling analysis of the quality of the sub-components.

The sample was sintered at a lower temperature of 1450 °C, so the zirconia is expected to be denser than the alumina segment (normally sintered at 1600 °C). This peculiarity of material density can be confirmed by the porosity map shown in Fig. 8c. Thus, the central zirconia star looks darker than its surroundings because there is less scattering in its volume. It should be noted, however, that the middle of the star is slightly brighter. This imaging artifact can be explained by the wavy shape of the sample. Normal reflection in certain parts of the sample increased the signal, which affected the image of the porosity map. Despite this, the components can be easily distinguished.

The B-scan of the sample (see Fig. 8e for details) reveal the 3D printed layers and their shape for both components (10 layers detected

for this sintered part). The average layer thickness of around 31 μm is estimated. A B-scan of the same region, recorded with the aforementioned commercial system at the 1.3 μm central wavelength is shown in Fig. 8f for comparison. This scatter-limited cross-sectional scan reveals no relevant sub-surface information; one layer is weakly detected for the zirconia component. Nevertheless, scattering variations are observed.

The results of OCT measurements of the green two-component copper-glass ceramic sample are summarized in Fig. 9. Fig. 9a shows an en-face scan of the top surface of the sample, which revealed some surface imperfections such as small bubbles and scratches. A frontal image of the conductive tracks taken at the depth of around 100 μm is shown in Fig. 9b. Since the copper particles are embedded in the polymer matrix, this layer exhibits strong scattering of the probing light, so the layer is clearly visible. No significant defects can be distinguished at this layer. However, a scan of the layer face below the conductive structure (Fig. 9c) reveals minor defects in the copper that locally (in the form of bubbles) penetrate the underlying glass-ceramic layers.

The origin of the defects is similar to the disk sample: during printing, air cannot always be effectively removed from under the sample due to the lateral size of the latter.
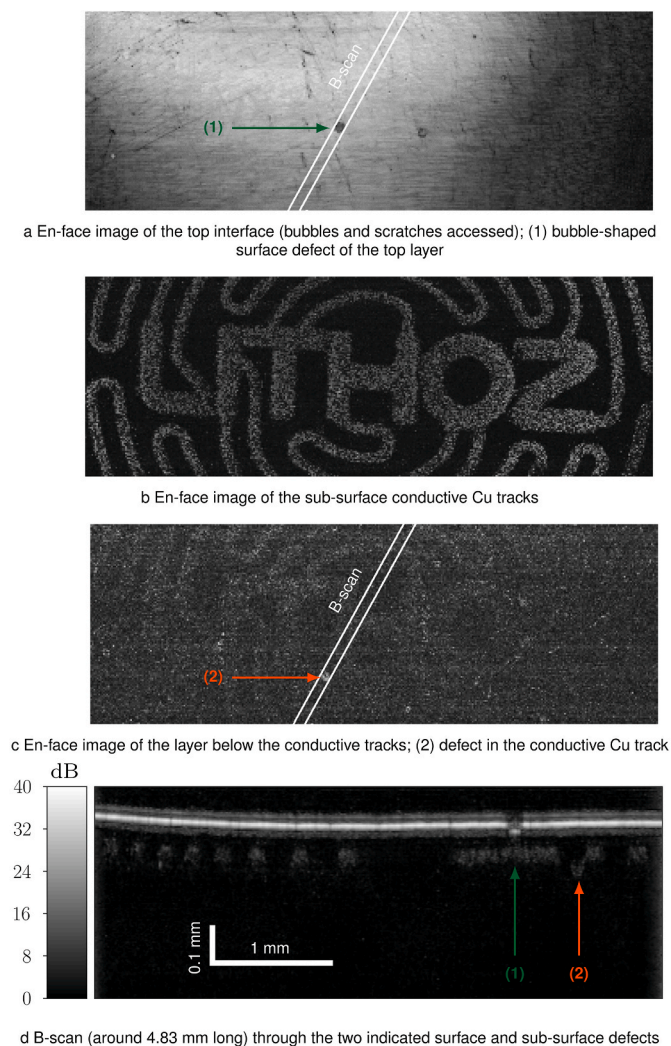
a En-face image of the top interface (bubbles and scratches accessed); (1) bubble-shaped surface defect of the top layer

b En-face image of the sub-surface conductive Cu tracks

c En-face image of the layer below the conductive tracks; (2) defect in the conductive Cu track

d B-scan (around 4.83 mm long) through the two indicated surface and sub-surface defects

Fig. 9. OCT examination of the Cu/Glass ceramic 2-component green part; a volumetric scan of 14×5 mm^2 is analyzed in (a–c).

Fig. 9d depicts a B-scan of the sample made through both defects (numbered for the sake of clarity) at an angle of 56°(overall length is around 4.83 mm). The copper-containing layer as well as the defects can be identified. In contrast to some OCT studies of green parts presented above, no layers were distinguished in the glass-ceramic specimen, indicating that the material properties—when attributed to optical properties—are quite homogeneous.

4. Discussions

The field of ceramic additive manufacturing is experiencing dynamic growth, with a large number of new solutions, printing methods, materials and approaches emerging rapidly. All research as well as already well-established industrial applications require rational inspection quality control methods. Since ceramic materials possess high scattering, most standard methods suitable, for example, for additive polymer production are not feasible in this case.

Recently, it has been proven that novel mid-IR OCT is well suited for ceramic materials. This non-destructive non-contact volumetric imaging technique, which does not require any sample preparation, provides rational and sufficient—in most cases—probing into scattering materials, high spatial resolution (at the scale of the printing machine or higher), and high sensitivity. Therefore, we demonstrate that mid-IR OCT is a suitable and very promising method for ceramic additive

manufacturing. Mid-IR OCT provides appropriate capabilities for multidimensional structural or functional investigation and defectoscopy of 3D printed ceramic parts. We emphasize that it can be a stand-alone method as well as an complementary modality.

As shown in our study, the structure and various properties of 3D printed ceramics can be directly accessed and studied using mid-IR OCT. In order to demonstrate the practical capabilities of the method, experimental verification and defectoscopy exemplified by the most common production faults were provided. The relevance of the performed non-destructive evaluation of typical defects is of high practical importance. Thus, for instance, detected cracks and bubbles reduce the mechanical stability of the part and can cause a more serious defect formation during sintering (e.g., breakage, designed geometry mismatch). The porosity mapping carried out provides a localized analysis of density changes. The porosity variations can also be undesirable and negatively affect material properties (resulting, for example, in reduced or uncontrolled bending and tensile strength, thermal stability, etc.). In addition to direct morphological information, it can be seen that, for example, layer visibility and probing depth depend on the sample, material or production parameters. Thus, advanced processing techniques or targeted analysis of printing parameters or material studies are feasible and can potentially enable new insights into printing processes. For example, a rigorous calibration of the porosity mapping procedure using components with well-defined densities could potentially allow us to perform quantitative porosity mapping. The objective of this contribution is to introduce and demonstrate the methods provided by mid-IR OCT to a wide range of experts and researchers involved in the additive production of ceramics.

Considering possible improvements, we envision future optimization of the mid-IR OCT system in terms of imaging speed and sensitivity. These properties are in focus because they are the most technically challenging, unlike, for example, spatial resolution, which can be improved either by replacing the optics (lateral) or by expanding the bandwidth (axial). Current imaging speed limits some application scenarios (e.g. dynamic processes) since volumetric scans appear time-consuming. The use of more stable emitters and faster spectral scanners will allow us to improve the scan rate performance significantly. At the same time, advances in supercontinuum sources [65] and mid-IR detector technologies provide options for increasing OCT sensitivity, which will enable the detection of fainter reflectors and increase penetration depth. Hence, further improvements in mid-IR OCT imaging performance are expected. In addition, the development of mid-IR optical technology promises improved availability and quality of optical components, as well as lower system costs.

5. Conclusions

In this study, the imaging capabilities and operational performance of a novel non-destructive testing technique of mid-infrared optical coherence tomography (mid-IR OCT) were demonstrated for quality assurance of additively manufactured ceramics. The developed mid-IR OCT was applied for at-line volumetric structural imaging and examination of various green and sintered 3D printed components (porous and dense alumina, zirconia, glass- and copper-ceramics, multi-component specimens). The selected samples were successfully investigated, and various structural features and defects (e.g., bubble defects, printed layer defects, porosity changes) were identified.

Thus, relying on experimental data, we discuss potential use cases of interest in this particular application area. Besides, the comparison with state-of-the-art solutions supplemented our discussions and highlighted the advanced capabilities of OCT in the mid-IR spectral range.

The developed system is designed to be simple and ready to use in the field conditions, as it does not impose any special requirements other than laser safety. The form factor of the system has been adapted with the prospect of integrating the OCT measurement head into a 3D ceramic printer for in-line process monitoring and quality control during

printing. Such a solution can offer a number of advantages in future. In-line inspection allows direct monitoring of layer growth, verification of geometry (e.g., thickness and compliance with CAD designs), measurement of roughness and porosity, and monitoring of defect development with real-time recognition as part of a user warning system [66]. In-line monitoring can make production chains more efficient by detecting potential defects faster, which saves in the end time and costs. We see such integration as a future potential development stage.

In addition, it should be noted that the capabilities of mid-IR OCT are not limited to AM ceramics, we expect its adaptation for associated areas related to the direct production, sintering, and quality control of industrial and domestic ceramics.

Acknowledgments

References

[1] Z. Chen, Z. Li, J. Li, C. Liu, C. Lao, Y. Fu, C. Liu, Y. Li, P. Wang, Y. He, 3d printing of ceramics: a review, J. Eur. Ceram. Soc. 39 (4) (2019) 661–687, https://doi.org/10.1016/j.jeurceramsoc.2018.11.013. URL, https://www.sciencedirect.com/science/article/pii/S0955221918306782.

[2] R.L. Walton, E.R. Kupp, G.L. Messing, Additive manufacturing of textured ceramics: a review, J. Mater. Res. 36 (18) (2021) 3591–3606, https://doi.org/10.1557/s43578-021-00283-6. URL, https://link.springer.com/10.1557/s43578-021-00283-6.

[3] F. Zhang, Z. Li, M. Xu, S. Wang, N. Li, J. Yang, A review of 3d printed porous ceramics, J. Eur. Ceram. Soc. 42 (8) (2022) 3351–3373, https://doi.org/10.1016/j.jeurceramsoc.2022.02.039. URL, https://www.sciencedirect.com/science/article/pii/S0955221922001406.

[4] L.C. Hwa, S. Rajoo, A.M. Noor, N. Ahmad, M. Uday, Recent advances in 3d printing of porous ceramics: a review, Curr. Opin. Solid State Mater. Sci. 21 (6) (2017) 323–347, https://doi.org/10.1016/j.cossms.2017.08.002. URL, https://www.sciencedirect.com/science/article/pii/S1359028616301723.

[5] J.-C. Wang, H. Dommati, S.-J. Hsieh, Review of additive manufacturing methods for high-performance ceramic materials, Int. J. Adv. Manuf. Technol. 103 (5–8) (2019) 2627–2647, https://doi.org/10.1007/s00170-019-03669-3. URL, http://link.springer.com/10.1007/s00170-019-03669-3.

[6] E.R. Cholleti, A review on 3d printing of piezoelectric materials, IOP Conf. Ser. Mater. Sci. Eng. 455 (2018), 012046, https://doi.org/10.1088/1757-899x/455/1/012046. URL, https://doi.org/10.1088/1757-899x/455/1/012046.

[7] S. XiaoHui, L. Wei, S. PingHui, S. QingYong, W. QingSong, S. YuSheng, L. Kai, L. WenGuang, Selective laser sintering of aliphatic-polycarbonate/hydroxyapatite composite scaffolds for medical applications, Int. J. Adv. Manuf. Technol. 81 (1–4) (2015) 15–25, https://doi.org/10.1007/s00170-015-7135-x. URL, http://link.springer.com/10.1007/s00170-015-7135-x.

[8] F. Scalera, C. Esposito Corcione, F. Montagna, A. Sannino, A. Maffezzoli, Development and characterization of uv curable epoxy/hydroxyapatite suspensions for stereolithography applied to bone tissue engineering, Ceram. Int. 40 (10, Part A) (2014) 15455–15462, https://doi.org/10.1016/j.ceramint.2014.06.117. URL, https://www.sciencedirect.com/science/article/pii/S0272884214010165.

[9] A. Paterlini, A. Stamboulis, V. Turq, R. Laloo, M. Schwentenwein, D. Brouczek, M. Piccinini, G. Bertrand, Lithography-based manufacturing of advanced ceramics for orthopaedic applications: a comparative tribological study, Open Ceramics 8 (2021), 100170, https://doi.org/10.1016/j.oceram.2021.100170. URL, https://www.sciencedirect.com/science/article/pii/S2666539521001164.

[10] R. Galante, C.G. Figueiredo-Pina, A.P. Serro, Additive manufacturing of ceramics for dental applications: a review, Dent. Mater. 35 (6) (2019) 825–846, https://doi.org/10.1016/j.dental.2019.02.026. URL, https://www.sciencedirect.com/science/article/pii/S0109564118304263.

[11] D. Kluess, P. Bergschmidt, W. Mittelmeier, R. Bader, 5 - ceramics for joint replacement*note: this chapter is an updated version of chapter 7 from the first edition of joint replacement technology edited by p. a. revell and published by woodhead publishing 2008*, second edition Edition, in: P. Revell (Ed.), Joint Replacement Technology, second ed., Woodhead Publishing, 2014, pp. 152–166, https://doi.org/10.1533/9780857098474.2.152. URL, https://www.sciencedirect.com/science/article/pii/B9780857098412500059.

[12] B. Bal, M. Rahaman, Orthopedic applications of silicon nitride ceramics, Acta Biomater. 8 (8) (2012) 2889–2898, https://doi.org/10.1016/j.actbio.2012.04.031. URL, https://www.sciencedirect.com/science/article/pii/S174270611200178X.

[13] F. Lusquiños, J. del Val, F. Arias-González, R. Comesaña, F. Quintero, A. Riveiro, M. Boutinguiza, J.R. Jones, R.G. Hill, J. Pou, Bioceramic 3d implants produced by laser assisted additive manufacturing, Phys. Procedia 56 (2014) 309–316, https://doi.org/10.1016/j.phpro.2014.08.176, 8th International Conference on Laser Assisted Net Shape Engineering LANE 2014. URL, https://www.sciencedirect.com/science/article/pii/S1875389214003216.

[14] J. Parthasarathy, 3D modeling, custom implants and its future perspectives in craniofacial surgery, Annal Maxillofacial Surg. 4 (1) (2014) 9, https://doi.org/10.4103/2231-0746.133065. URL, http://www.amsjournal.com/text.asp?2014/4/1/9/133065.

[15] W. Chen, S. Kirihara, Y. Miyamoto, Fabrication and measurement of micro three-dimensional photonic crystals of sio2 ceramic for terahertz wave applications, –2081, J. Am. Ceram. Soc. 90 (7) (2007) 2078, https://doi.org/10.1111/j.1551-2916.2007.01676.x. URL, https://ceramics.onlinelibrary.wiley.com/doi/abs/10.1111/j.1551-2916.2007.01676.x.

[16] S. Kirihara, T. Niki, Three-dimensional stereolithography of alumina photonic crystals for terahertz wave localization, Int. J. Appl. Ceram. Technol. 12 (1) (2015) 32–37, https://doi.org/10.1111/ijac.12320. URL, https://ceramics.onlinelibrary.wiley.com/doi/abs/10.1111/ijac.12320.

[17] X. Lu, Y. Lee, S. Yang, Y. Hao, J.R. Evans, C.G. Parini, Solvent-based paste extrusion solid freeforming, J. Eur. Ceram. Soc. 30 (1) (2010) 1–10, https://doi.org/10.1016/j.jeurceramsoc.2009.07.019. URL, https://www.sciencedirect.com/science/article/pii/S0955221909003860.

[18] N.T. Nguyen, N. Delhote, M. Ettorre, D. Baillargeat, L. Le Coq, R. Sauleau, Design and characterization of 60-ghz integrated lens antennas fabricated through ceramic stereolithography, IEEE Trans. Antenn. Propag. 58 (8) (2010) 2757–2762, https://doi.org/10.1109/TAP.2010.2050447.

[19] S. Leigh, C. Purssell, J. Bowen, D. Hutchins, J. Covington, D. Billson, A miniature flow sensor fabricated by micro-stereolithography employing a magnetite/acrylic nanocomposite resin, Sensor Actuator Phys. 168 (1) (2011) 66–71, https://doi.org/10.1016/j.sna.2011.03.058. URL, https://www.sciencedirect.com/science/article/pii/S0924424711002287.

[20] P. Sarobol, A. Cook, P.G. Clem, D. Keicher, D. Hirschfeld, A.C. Hall, N.S. Bell, Additive manufacturing of hybrid circuits, arXiv:https://doi.org/10.1146/annurev-matsci-070115-031632, Annu. Rev. Mater. Res. 46 (1) (2016) 41–62, https://doi.org/10.1146/annurev-matsci-070115-031632. URL, https://doi.org/10.1146/annurev-matsci-070115-031632.

[21] R. Liu, Z. Wang, T. Sparks, F. Liou, J. Newkirk, Aerospace applications of laser additive manufacturing, in: M. Brandt (Ed.), Laser Additive Manufacturing, Woodhead Publishing Series in Electronic and Optical Materials, Woodhead Publishing, 2017, pp. 351–371, https://doi.org/10.1016/B978-0-08-100433-3.00013-0. URL, https://www.sciencedirect.com/science/article/pii/B9780081004333000130.

[22] N. Travitzky, Processing of ceramic–metal composites, Adv. Appl. Ceram. 111 (5–6) (2012) 286–300, https://doi.org/10.1179/1743676111Y.0000000073. URL, https://doi.org/10.1179/1743676111Y.0000000073.

[23] N. Travitzky, A. Bonet, B. Dermeik, T. Fey, I. Filbert-Demut, L. Schlier, T. Schlordt, P. Greil, Additive manufacturing of ceramic-based materials, Adv. Eng. Mater. 16 (6) (2014) 729–754, https://doi.org/10.1002/adem.201400097. URL, https://onlinelibrary.wiley.com/doi/abs/10.1002/adem.201400097.

[24] W. Zhou, R. Apkarian, Z.L. Wang, D. Joy, Fundamentals of scanning electron microscopy (sem), in: W. Zhou, Z.L. Wang (Eds.), Scanning Microscopy for Nanotechnology: Techniques and Applications, Springer New York, New York, NY, 2007, pp. 1–40, https://doi.org/10.1007/978-0-387-39620-0_1. URL.

[25] J. Kastner, C. Heinzl, X-ray computed tomography for non-destructive testing and materials characterization, in: Z. Liu, H. Ukida, P. Ramuhalli, K. Niel (Eds.), Integrated Imaging and Vision Techniques for Industrial Inspection: Advances and Applications, Springer London, London, 2015, pp. 227–250. https://doi.org/10.1007/978-1-4471-6741-9_8.

[26] B. Heise, S.E. Schausberger, S. Häuser, B. Plank, D. Salaberger, E. Leiss-Holzinger, D. Stifter, Full-field optical coherence microscopy with a sub-nanosecond supercontinuum light source for material research, fiber Supercontinuum sources and their applications, Opt. Fiber Technol. 18 (5) (2012) 403–410, https://doi.org/10.1016/j.yofte.2012.07.011. URL, https://www.sciencedirect.com/science/article/pii/S106852001200082X.

[27] D.B. Murphy, M.W. Davidson, Fundamentals of Light Microscopy and Electronic Imaging, second ed., Wiley-Blackwell, Hoboken, N.J, 2013.

[28] W. Drexler, J.G. Fujimoto, Optical Coherence Tomography: Technology and Applications, second ed., Springer International Publishing Switzerland, Cham New York, 2015.

[29] S.H. Yun, G.J. Tearney, J.F. de Boer, N. Iftimia, B.E. Bouma, High-speed optical frequency-domain imaging, Opt Express 11 (22) (2003) 2953–2963, https://doi.org/10.1364/OE.11.002953. URL, http://www.opticsexpress.org/abstract.cfm?URI=oe-11-22-2953.

[30] S. Moon, D.Y. Kim, Ultra-high-speed optical coherence tomography with a stretched pulse supercontinuum source, Opt Express 14 (24) (2006) 11575–11584, https://doi.org/10.1364/OE.14.011575. URL, http://www.opticsexpress.org/abstract.cfm?URI=oe-14-24-11575.

[31] S. Tozburun, C. Blatter, M. Siddiqui, E.F.J. Meijer, B.J. Vakoc, Phase-stable Doppler oct at 19 mhz using a stretched-pulse mode-locked laser, Biomed. Opt Express 9 (3) (2018) 952–961, https://doi.org/10.1364/BOE.9.000952. URL, http://www.osapublishing.org/boe/abstract.cfm?URI=boe-9-3-952.

[32] T.S. Kim, J. Joo, I. Shin, P. Shin, W.J. Kang, B.J. Vakoc, W.-Y. Oh, 9.4 MHz A-line rate optical coherence tomography at 1300 nm using a wavelength-swept laser based on stretched-pulse active mode-locking, Sci. Rep. 10 (1) (2020) 9328, https://doi.org/10.1038/s41598-020-66322-0. URL, http://www.nature.com/articles/s41598-020-66322-0.

[33] J. Fujimoto, E. Swanson, The development, commercialization, and impact of optical coherence tomography, Invest. Opthalmol. Visual Sci. 57 (9) (2016) 1–13, https://doi.org/10.1167/iovs.16-19963. URL, http://iovs.arvojournals.org/article.aspx?doi=10.1167/iovs.16-19963.

[34] O.M. Carrasco-Zevallos, C. Viehland, B. Keller, M. Draelos, A.N. Kuo, C.A. Toth, J. A. Izatt, Review of intraoperative optical coherence tomography: technology and applications <display>\begin{equation*}invited\end{equation*}</display>, Biomed. Opt Express 8 (3) (2017) 1607–1637, https://doi.org/10.1364/BOE.8.001607. URL, http://opg.optica.org/boe/abstract.cfm?URI=boe-8-3-1607.

[35] D. Stifter, Beyond biomedicine: a review of alternative applications and developments for optical coherence tomography, Appl. Phys. B 88 (3) (2007) 337–357, https://doi.org/10.1007/s00340-007-2743-2. URL, https://doi.org/10.1007/s00340-007-2743-2.

[36] B. Heise, B. Buchroithner, S.E. Schausberger, P. Hierzenberger, G. Eder, D. Stifter, Simultaneous detection of optical retardation and axis orientation by polarization-sensitive full-field optical coherence microscopy for material testing, Laser Phys. Lett. 11 (5) (2014), 055602, https://doi.org/10.1088/1612-2011/11/5/055602. URL, https://doi.org/10.1088/1612-2011/11/5/055602.

[37] B. Heise, G. Hannesschlaeger, E. Leiss-Holzinger, L. Peham, I. Zorin, Optical coherence tomography in nondestructive testing, in: P.J. de Groot, R.K. Leach, P. Picart (Eds.), Optics and Photonics for Advanced Dimensional Metrology, vol. 11352, International Society for Optics and Photonics, SPIE, 2020, pp. 227–232, https://doi.org/10.1117/12.2556832. URL, https://doi.org/10.1117/12.2556832.

[38] P. Targowski, M. Iwanicka, Optical Coherence Tomography: its role in the non-invasive structural examination and conservation of cultural heritage objects—a review, Appl. Phys. A 106 (2) (2012) 265–277, https://doi.org/10.1007/s00339-011-6687-3. URL, http://link.springer.com/10.1007/s00339-011-6687-3.

[39] M. Bashkansky, P.R. Battle, M.D. Duncan, M. Kahn, J. Reintjes, Subsurface defect detection in ceramics using an optical gated scatter reflectometer, J. Am. Ceram. Soc. 79 (5) (1996) 1397–1400, https://doi.org/10.1111/j.1151-2916.1996.tb08602.x. URL, https://ceramics.onlinelibrary.wiley.com/doi/abs/10.1111/j.1151-2916.1996.tb08602.x.

[40] F. Sakamoto, T. Takahashi, J. Tatami, M. Iijima, Prediction of strength based on defect analysis in Al_2O_3 ceramics via non-destructive and three-dimensional observation using optical coherence tomography, J. Ceram. Soc. Jpn. 127 (7) (2019) 462–468, https://doi.org/10.2109/jcersj2.19020. URL, https://www.jstage.jst.go.jp/article/jcersj2/127/7/127_19020/_article.

[41] C. Wunderlich, B. Bendjus, M. Kopycinska-Müller, Nde in additive manufacturing of ceramic components, in: N. Meyendorf, N. Ida, R. Singh, J. Vrana (Eds.), Handbook of Nondestructive Evaluation 4.0, Springer International Publishing, Cham, 2021, pp. 1–19, https://doi.org/10.1007/978-3-030-48200-8_15-1. URL.

[42] S. Toyokura, Contactless mapping of ceramic green density using optical coherence tomography, Open Ceramics 5 (2021), 100061, https://doi.org/10.1016/j.oceram.2021.100061. URL, https://www.sciencedirect.com/science/article/pii/S2666539521000079.

[43] R. Su, M. Kirillin, E.W. Chang, E. Sergeeva, S.H. Yun, L. Mattsson, Perspectives of mid-infrared optical coherence tomography for inspection and micrometrology of industrial ceramics, Opt Express 22 (13) (2014) 15804–15819, https://doi.org/10.1364/OE.22.015804. URL, http://www.opticsexpress.org/abstract.cfm?URI=oe-22-13-15804.

[44] H. Kitahara, M. Tani, M. Hangyo, Frequency-domain optical coherence tomography system in the terahertz region, Appl. Phys. B 126 (1) (2020) 22, https://doi.org/10.1007/s00340-019-7371-0. URL, http://link.springer.com/10.1007/s00340-019-7371-0.

[45] H. Hulst, H. van de Hulst, Light Scattering by Small Particles, Dover Books on Physics, Dover Publications, 1981.

[46] C. Bohren, D. Huffman, Absorption and Scattering of Light by Small Particles, Wiley Science Series, Wiley, 2008.

[47] I. Zorin, R. Su, A. Prylepa, J. Kilgus, M. Brandstetter, B. Heise, Mid-infrared fourier-domain optical coherence tomography with a pyroelectric linear array, Opt Express 26 (25) (2018) 33428–33439, https://doi.org/10.1364/OE.26.033428. URL, http://www.opticsexpress.org/abstract.cfm?URI=oe-26-25-33428.

[48] N.M. Israelsen, C.R. Petersen, A. Barh, D. Jain, M. Jensen, G. Hannesschläger, P. Tidemand-Lichtenberg, C. Pedersen, A. Podoleanu, O. Bang, Real-time high-resolution mid-infrared optical coherence tomography, Light Sci. Appl. 8 (11) (2019) 2047–7538, https://doi.org/10.1038/s41377-019-0122-5. URL, https://doi.org/10.1038/s41377-019-0122-5.

[49] I. Zorin, R. Su, B. Heise, B. Lendl, M. Brandstetter, Correlative infrared optical coherence tomography and hyperspectral chemical imaging, J. Opt. Soc. Am. 37

[50] I. Zorin, J. Kilgus, R. Su, B. Lendl, M. Brandstetter, B. Heise, Multimodal mid-infrared optical coherence tomography and spectroscopy for non-destructive testing and art diagnosis, in: H. Liang, R. Groves, P. Targowski (Eds.), Optics for Arts, Architecture, and Archaeology VII, vol. 11058, International Society for Optics and Photonics, SPIE, 2019, pp. 74–88, https://doi.org/10.1117/12.2528279. URL, https://doi.org/10.1117/12.2528279.

[51] I. Zorin, P. Gattinger, M. Brandstetter, B. Heise, Dual-band infrared optical coherence tomography using a single supercontinuum source, Opt Express 28 (6) (2020) 7858–7874, https://doi.org/10.1364/OE.386398. URL, http://www.opticsexpress.org/abstract.cfm?URI=oe-28-6-7858.

[52] A. Vanselow, P. Kaufmann, I. Zorin, B. Heise, H.M. Chrzanowski, S. Ramelow, Frequency-domain optical coherence tomography with undetected mid-infrared photons, Optica 7 (12) (2020) 1729–1736, https://doi.org/10.1364/OPTICA.400128. URL, http://www.osapublishing.org/optica/abstract.cfm?URI=optica-7-12-1729.

[53] N.M. Israelsen, P.J. Rodrigo, C.R. Petersen, G. Woyessa, R.E. Hansen, P. Tidemand-Lichtenberg, C. Pedersen, O. Bang, High-resolution mid-infrared optical coherence tomography with khz line rate, Opt. Lett. 46 (18) (2021) 4558–4561, https://doi.org/10.1364/OL.432765. URL, http://opg.optica.org/ol/abstract.cfm?URI=ol-46-18-4558.

[54] C.R. Petersen, N. Rajagopalan, C. Markos, N.M. Israelsen, P.J. Rodrigo, G. Woyessa, P. Tidemand-Lichtenberg, C. Pedersen, C.E. Weinell, S. Kiil, O. Bang, Non-destructive subsurface inspection of marine and protective coatings using near- and mid-infrared optical coherence tomography, Coatings 11 (8) (2021), https://doi.org/10.3390/coatings11080877. URL, https://www.mdpi.com/2079-6412/11/8/877.

[55] I. Zorin, P. Gattinger, A. Prylepa, B. Heise, Time-encoded mid-infrared fourier-domain optical coherence tomography, Opt. Lett. 46 (17) (2021) 4108–4111, https://doi.org/10.1364/OL.434855. URL, http://opg.optica.org/ol/abstract.cfm?URI=ol-46-17-4108.

[56] H. Gheisari, E. Karamian, M. Abdellahi, A novel hydroxyapatite –hardystonite nanocomposite ceramic, Ceram. Int. 41 (4) (2015) 5967–5975, https://doi.org/10.1016/j.ceramint.2015.01.033. URL, https://www.sciencedirect.com/science/article/pii/S0272884215000723.

[57] A.M. Hofmeister, K.M. Pitman, A.F. Goncharov, A.K. Speck, Optical constants of silicon carbide for astrophysical applications. ii. extending optical functions from infrared to ultraviolet using single-crystal absorption spectra, Astrophys. J. 696 (2) (2009) 1502–1516, https://doi.org/10.1088/0004-637x/696/2/1502. URL, https://doi.org/10.1088/0004-637x/696/2/1502.

[58] M. Manoj, D. Mangalaraj, N. Ponpandian, C. Viswanathan, Core–shell hydroxyapatite/mg nanostructures: surfactant free facile synthesis, characterization and their in vitro cell viability studies against leukaemia cancer cells (k562), RSC Adv. 5 (2015) 48705–48711, https://doi.org/10.1039/C5RA04663G. URL, http://dx.doi.org/10.1039/C5RA04663G.

[59] G. Scardera, T. Puzzer, G. Conibeer, M.A. Green, Fourier transform infrared spectroscopy of annealed silicon-rich silicon nitride thin films, J. Appl. Phys. 104 (10) (2008), 104310, https://doi.org/10.1063/1.3021158 arXiv:https://doi.org/10.1063/1.3021158. URL, https://doi.org/10.1063/1.3021158.

[60] S. Nohut, S. Geier, I. Kraleva, M. Schwentenwein, R. Bermejo, Lithography-based additive manufacturing of porosity graded alumina, Add. Manufacture Lett. 3 (2022), 100060, https://doi.org/10.1016/j.addlet.2022.100060. URL, https://www.sciencedirect.com/science/article/pii/S2772369022000342.

[61] L. Yuan, B. Liu, N. Shen, T. Zhai, D. Yang, Synthesis and properties of borosilicate/aln composite for low temperature co-fired ceramics application, J. Alloys Compd. 593 (2014) 34–40, https://doi.org/10.1016/j.jallcom.2014.01.074. URL, https://www.sciencedirect.com/science/article/pii/S0925838814001054.

[62] E. Hamzawy, A. El-Kheshen, M. Zawrah, Densification and properties of glass/cordierite composites, Ceram. Int. 31 (3) (2005) 383–389, https://doi.org/10.1016/j.ceramint.2004.06.003. URL, https://www.sciencedirect.com/science/article/pii/S0272884204003670.

[63] M. Lima, R. Monteiro, M. Graça, M. Ferreira da Silva, Structural, electrical and thermal properties of borosilicate glass–alumina composites, J. Alloys Compd. 538 (2012) 66–72, https://doi.org/10.1016/j.jallcom.2012.05.024. URL, https://www.sciencedirect.com/science/article/pii/S0925838812008328.

[64] I.H. Malitson, F.V. Murphy, W.S. Rodney, Refractive index of synthetic sapphire, J. Opt. Soc. Am. 48 (1) (1958) 72–73, https://doi.org/10.1364/JOSA.48.000072. URL, http://opg.optica.org/abstract.cfm?URI=josa-48-1-72.

[65] I. Zorin, P. Gattinger, A. Ebner, M. Brandstetter, Advances in mid-infrared spectroscopy enabled by supercontinuum laser sources, Opt Express 30 (4) (2022) 5222–5254, https://doi.org/10.1364/OE.447269. URL, http://opg.optica.org/oe/abstract.cfm?URI=oe-30-4-5222.

[66] R. Zvagelsky, F. Mayer, D. Beutel, C. Rockstuhl, G. Gomard, M. Wegener", Towards *in-situ* diagnostics of multi-photon 3d laser printing using optical coherence tomography, Light: Adv. Manuf. 3 (LAM2022030008) (2022) 1, https://doi.org/10.37188/lam.2022.039. URL, https://www.light-am.com//article/id/5a169306-ee11-44ed-b4ff-fdfb765ec1ae.